2-9-2022

Seismic Interferometry using Seismic Noise from Wind Turbines and other Anthropogenic Sources

Mitchell A. Spangler
Purdue University, spangle4@purdue.edu

Robert L. Nowack
Purdue University, nowack@purdue.edu

Seismic Interferometry using Seismic Noise from Wind Turbines and other Anthropogenic Sources

Mitchell A. Spangler[1] and Robert L. Nowack[1]

[1] Purdue University, Department of Earth, Atmospheric and Planetary Sciences,

West Lafayette, IN, 47906, USA. E-mail: mitchspang@gmail.com, nowack@purdue.edu

Date: February 9, 2022

GeoData Science MS Presentation

Abstract

We investigate seismic noise from anthropogenic sources, in particular wind turbines, for seismic interferometry. The data is from the 17-station Autocorr Seismic Array located in the Midwestern United States. The array has a linear component that extends about 30 km from north to south and a subarray to the south with a diameter of 10 km. The array was deployed from August 2019 to July 2020, which included the initial months of the Covid-19 pandemic. The northernmost seismic stations of the array are located within the southern end of one of the largest onshore wind farms in the world. To the south of the array there are regularly occurring east-west running trains. However even during times when trains are present, the frequency signatures of the wind turbines are dominant over much of the array, including seismic stations well to the south of the wind farm. Although there is vehicle traffic in the region, time windows in the late evening and early morning were chosen to reduce its effect. Shallow refraction data are available nearby individual seismic stations of the array, and since the spectral peaks do not vary for stations with differing basement depths, they are inferred to be source effects of wind turbines. When utilizing seismic interferometry, coherent Rayleigh wave signals are observed for time windows of seismic noise as short as 15 minutes. There are also concurrent estimates of average hourly wind speeds and wind gusts at the locations of the seismic stations. These data show that for ambient noise correlations, clear south propagating Rayleigh waves are observed for moderate to large average hourly wind speeds. For lower wind speeds, less coherent Rayleigh wave signals are observed in the one-hour ambient noise correlations. For seismic stations within the wind farm, both north and south propagating Rayleigh waves are observed in the correlations. However, for seismic stations to the south of the wind farm, only south propagating waves are observed, which are inferred to be coming from the wind farm.

1. Introduction

In this study, we investigate anthropogenic seismic noise, in particular from wind turbines, recorded by the Autocorr Seismic Array. The array consists of 17 stations and was deployed from August 2019 to July 2020 near West Lafayette, Indiana in the Midwest region of the United States. The array has a linear component that extends about 30 km from north to south and a subarray to the south with a diameter of 10 km. To the south of the array, there is east-west running train tracks with regularly occurring trains. The northernmost stations in the array are within the southern part one of the largest combined onshore wind farms in the world (NS Energy, 2019). There are also smaller roads, as well as several larger roads, in the broader region of the array.

The successful study of the seismic wavefields requires the identification of not only natural sources, but also the ability to delineate anthropogenic sources (Seydoux et al., 2016; Meng et al., 2019). An important source of anthropogenic noise is from wind turbines. According to Lerbs et al. (2020), wind turbines are often placed in more remote regions to reduce their effects on the general public. Also, they can interfere with seismic instrumentation designed to record signals for other purposes, such as for the study of remote earthquakes or distant controlled sources. Styles et al. (2005) investigated wind turbine signals recorded on seismic sensors and found characteristic resonance frequencies of the wind turbines. Stammler and Ceranna (2016), Ziegler and Ritter (2017) and Hu et al. (2019) identified sharp frequency peaks from wind turbines between 1 and 10 Hz. Limberger et al. (2021) estimated the seismic spectral amplitudes from wind turbines decay as power laws with distance from the wind turbines. Westwood and Styles (2017) utilized polarization analysis to show that the seismic signals emitted by wind turbines are mostly Rayleigh waves. Friedrich et al. (2018) inferred that although the major source of vibrations from the wind turbines are the rotor blades passing the tower, this then results in the excitation of

eigenfrequencies of modes of the tower, and this then couples to the ground to generate seismic waves. Neuffer et al. (2021) also inferred that the seismic signals emitted from wind turbines are related to eigenmodes of the wind turbine tower. Neuffer et al. (2019) found that for wind turbines with variable rotor speeds, spectral peaks recorded at seismic stations directly attributable to blade pass frequencies are only observable near the tower foundation and less than about 1 km. For greater distances, spectral peaks did not vary even for different wind speeds and rotor speeds, suggesting that eigenmodes of the tower are responsible for these spectral peaks.

Stammler and Ceranna (2016) showed that spectral peaks from wind turbines are clearest when observed within several kilometers from a wind turbine and are no longer predominant at distances more than about 15 km. Neuffer et al. (2019) concluded that seismic signals from a large number of wind turbines increase as the square-root of the number of wind turbines. The range of observation from a large number of wind turbines would then correspondingly increase.

While wind is related to the seismic signals generated by wind turbines, wind itself also acts as a source of seismic noise. Withers et al. (1996) found that wind strongly affects the seismic background noise beginning at about 3 m/s. However, the effect of wind noise is reduced by deploying sensors at depth. Lott et al. (2017) showed a linear increase of the log power of the ground motion with increasing wind speed. Dybing et al. (2019) found that wind acts most strongly as a source of noise on the horizontal components, and less so on the vertical component.

Another source of anthropogenic noise is trains (Riahi and Gerstoft, 2015), which display prominent spectral peaks over a relatively large frequency range (Fuchs et al., 2017). While many studies, including by Lavoué et al. (2020) and Schippkus et al. (2020), have investigated signals within a few kilometers of a passing train, Pinzon-Rincon et al. (2021) inferred that train signals could be detectable out to much farther distances away from the train tracks.

Another source of anthropogenic noise is vehicle traffic. In the time domain, vehicles generate signals that resemble short duration seismic tremors and have characteristic spectrograms that are bell-shaped (Meng et al., 2021). Moreover, the spectrograms do not display as distinct spectral lines, distinguishing their spectral signature from other sources of anthropogenic noise (Schippkus et al., 2020).

Seismic interferometry using cross-correlation analysis can be used in order to extract seismic waves from ambient seismic noise (e.g. Shapiro et al., 2005; Wapenaar et al., 2008; and Nakata et al., 2019). More recently, it has been shown that it is possible to perform seismic interferometry using anthropogenic sources as well, such as from trains (Quiros et al., 2016) and wind turbines (Friedrich et al., 2018). Cars are also possible sources of noise for use with seismic interferometry, as they are recurring and avoid the need to set up expensive exploration seismic equipment (Lie et al., 2021). Friedrich et al. (2018) used seismic interferometry and also migration to locate wind turbines.

In this study, we will investigate sources of anthropogenic noise near the Autocorr Array. In particular, we will investigate wind turbines as a source of seismic noise and will also perform seismic interferometry on these data.

2 Data Analysis

2.1. The Autocorr Seismic Array

The Autocorr Seismic Array consists of 17 stations and was deployed from August 2019 to July 2020 west of West Lafayette, Indiana in the Midwestern United States and is shown in Figure 1. The seismic sensors of the Autocorr Array were Mark Products L-22 seismometers with a frequency of 2 Hz, and Reftek RT130 dataloggers. The instrument response was then removed

and corrected to velocity. The array is anchored at the southern end of the array by the N4 station, SFIN. The combined array has a linear north-south extent of approximately 30 kilometers. To the south of the array, there is a subarray that is about 10 kilometers in diameter, including the station SFIN. The northernmost stations ST14, ST15/17 and ST16 are situated within the southern part of a large wind farm. With more than 1,100 wind turbines, this wind farm is one of the largest onshore wind farms in the world, combined to include both Meadow Lakes and Fowler Ridge (NS Energy, 2019). The small dots in Figure 1 show the wind turbine locations closest to the seismic array, with additional wind turbines located farther north and to the west of the array. Also, stations ST15 and ST17 of the Autocorr Array occupied the same location but during different time periods.

To the south of the seismic array, there is an east-west running train tracks with trains operating on a regular daily basis. There are also a number of roads in the regional vicinity of the array, including I-65 located to the north and east of the array, US 52 crossing the central part of the array and US 231 running along the northern part of the array. In the southern part of the array, there are mostly smaller roads with more limited vehicle traffic. For this study, we will emphasize time periods during late night and early morning to reduce the effects of local vehicle traffic. The deployment duration of the array also included the first five months of the COVID-19 pandemic, when there was significantly reduced vehicle traffic on all roads in the region. Vehicle traffic and the effects of the COVID-19 pandemic on seismic noise will be investigated in a future study.

2.2. Wind Turbines and Train Signals

The Autocorr Seismic Array recorded several types of anthropogenic noise, including seismic signals from a large wind farm in which the northern part of the array is located, and regularly occurring trains on the east-west train tracks to the south of the array. Figure 2 shows examples of these two types of noise sources in the region. The vehicle traffic in the region

typically had very short time durations as a vehicle passed near by a given station and were less coherent over multiple stations. However, time periods in the late evening and early morning were used in this study to reduce its effects.

The wind turbine components that the northern portion of the seismic array was located within are the Meadow Lakes II and III projects. The wind turbine type for Meadow Lakes II is the Acciona AW-82/1500 model and the wind turbine type for Meadow Lake II is the GE 1.5/77 model. Figure 3 shows the power output for these two types of wind turbines. There is no power output from either model for wind speeds under about 2 m/s, and the power output is capped for wind speeds above 13 m/s and 14 m/s for the Acciona AW-82/1500 models and GE 1.5/77 models, respectively. Including rotors, the Acciona AW-82/1500 has a total height of 121 meters and a hub height of 80 meters, and the GE 1.5/77 is similar with a total height of 118.6 meters and a hub height of 80 meters. It was inferred by Neuffer et al. (2019, 2021) that the seismic signals emitted from wind turbines are mostly eigenfrequencies from modes of vibration of the towers themselves. While the seismic spectra at stations less than 1 km from the wind turbines may display spectral peaks related to the blade passing frequencies, the eigenmodes of the structures are what dominantly couple to the seismic ground motions in the field (Neuffer et al., 2019).

Trains are known to display distinct records on seismic spectrograms, first growing in strength as the train approaches and then decreasing as the train passes by (Lavoué et al., 2020, Rincon, 2021). On the train tracks to the south of the Autocorr Seismic Array, there are regularly occurring trains passing several times a day. An example video of a train passing to the south of the array is shown for June 24, 2020, at Turner Road near West Point, Indiana, which is several kilometers to the south of the Autocorr seismic array (see https://www.youtube.com/watch?v=C6DPwpF6X1Y.) Note that there appears to be a group of

avid train spotters in the area that periodically record trains at specific railroad crossings.

A 15-minute time window starting at 9:28 UTC December 22nd, 2019, contains a train passing to the south of the array. To investigate the signal, we first took the time series, and then computed the spectrogram and spectrum for seismic station ST01 as shown in Figure 4. Station ST01 was chosen because it is one of the southernmost stations located several kilometers to the north of the east-west train tracks. Figure 4a) shows the time series of the signal, 4b) shows a spectrogram and 4c) shows the spectrum, where the train signal at ST01 is clearly observed during this time period at this station. Although seismic signals from the train can be seen up to 25 Hz, the horizontal spectral peaks with time on the spectrogram from 16 to 20 Hz are likely due to other local sources of noise.

For stations farther to the north of the array, the train signals are no longer as evident in the records. For example, Figure 5 shows the time series, spectrogram, and spectrum for the same time period of December 22nd now for station ST12, which is in the middle of the linear component of the Autocorr Seismic Array. Figure 5a) displays the time series, Figure 5b) shows the spectrogram and 5c) show in the spectra for station ST12 for this same time period. There are now large, regularly spaced spectral peaks with a spacing of approximately 1 Hz up to about 12 Hz. There are also several peaks with time on the spectrogram between 18 and 22 Hz, which are likely due to other local sources of noise. In addition, there are localized vertical events in time likely due to due to cars or other sources of seismic noise. In any case, spectrogram and spectrum are now very different than the train spectral signals shown in Figure 4, with the train no longer the dominant signal for this station. This is also the case for seismic stations ST07, ST08, ST09 and for all stations farther to the north, which are greater than about 5-6 km away from the closest approach of the train (see Figure 1).

2.3. Regional Near-Surface Structure

From the map of physiographic regions of Indiana, the Autocorr Array is located within the Iroquois central till region (IGWS physiographic regions). The bedrock geology in the region of the array consists of Devonian rocks, where the upper portion are carbonaceous shales, and Mississippian rocks consisting of shales, sandstones, siltstones, limestones, and gypsums (IGWS bedrock).

Shallow seismic refraction data are available in Indiana from Whaley et al. (2002), and specifically for the region near the autocorr seismic array. Figure 6 shows the locations where these refraction data were recorded near the array and are given as small circles. Refraction data were dense in the southern portion of the seismic array and somewhat less dense in the northern part. The southern seismic stations therefore have more reliable refraction data to average, as well as having data points closer to each individual station. Throughout the entire seismic array, no refraction data were chosen that were more than 6 km away from a seismic station. The average distance for all the stations from the refraction locations to the stations was 2.6 km. Data were also selected based on data quality as given by Whaley et al. (2002). From these data, averages of the basement depths, and soil and basement P-wave velocities were obtained for each station and standard errors were computed. Table 1 summarizes the shallow seismic refraction statistics. The basement depths at selected seismic stations of the array are also shown in Figure 7.

Seismic refractions from an intermediate soil layer could result in the shallower depths estimated from the refraction data at ST15/17 and ST16, where there are also somewhat lower basement speeds than most of the other stations. SFIN also had a very shallow basement depth obtained from the seismic refraction data, but for this station there are visible basement outcrops within 200 m of the station. Based on the uncertainties given in Table 1 and Figure 7, the seismic

refraction data give stable basement depth estimates and also provide P-wave velocities for the soil layers and basement for the selected stations of the Autocorr Array.

2.4. Spectral Characteristics with Wind Speed

To investigate the seismic characteristics of the seismic stations when no trains are present, spectral analysis is performed on selected stations of the Autocorr Seismic Array. To calculate the amplitude spectra, the data is first detrended and a moving amplitude normalization in the time domain is performed. A bandpass filter from 0.5 to 15 Hz is applied and the data is detrended again. Next a 10% Tukey window is applied, and the data is zero padded to the next power of 2. The Fourier transform of the filtered and amplitude normalized data is then applied to obtain the spectra.

One-hour blocks of data were chosen for April 14th, April 27th, and April 30th of 2020 for seismic station ST12. These hour-long time windows were selected based on different wind speeds and wind gusts. These windows were also specified at 4 AM EST, when vehicle traffic and other anthropogenic noise were significantly lower. Also, the times were chosen during the first full month of the COVID-19 pandemic to further reduce vehicle traffic. The hour on April 30th had an average wind speed of 5.86 m/s and a wind gust of 11.31 m/s, the hour on April 14th had an average wind speed of 2.54 m/s and a wind gust of 4.45 m/s and the hour on April 27th had an average wind speed of 0.79 m/s and a wind gust of 1.01 m/s. The weather data were extracted from the DarkSky database which are interpolated to seismic station locations. Referring to Figure 3, a wind speed of less than 2 m/s resulted in no power output from the wind turbines. The power output then increased with increasing wind speed as shown in Figure 3. Figure 8 shows the different amplitude spectra. The spectrum on April 30th with a high wind speed clearly displays spectral peaks with about a 1 Hz spacing up to about 12 Hz. The spectrum on April 14th with a medium wind speed

displays a clear peak at 2.8 Hz and spectral peaks up to about 6 Hz. The spectrum on April 27th with low wind speed displays no spectral peaks, with even the 2.8 Hz peak no longer present. These data indicate that the spectral signatures become more pronounced in amplitude and for higher frequencies as wind speed increases, and are therefore not related to other anthropogenic sources such as vehicle traffic.

Figure 9 shows the amplitude spectra for one hour on April 30th, 2020, starting at 4 AM EST for selected stations in the Autocorr Array. This hour had a high average wind speed of 5.86 m/s and a wind gust of 11.31 m/s at central station ST12. The development of the spectral peaks is more pronounced for stations closer to the wind farm and less pronounced for stations farther away. Figure 9 also shows that the frequency of these peaks does not vary significantly with station location and even result in spectral peaks at the southernmost stations of the array. Note there is no train signal for this time window. Dashed lines are drawn at approximately 2.8 Hz and 6.8 Hz to demonstrate this stability of the spectral peaks. The peak at 6.8 Hz is less evident for the stations ST16 and ST15/17 where these stations are completely within the wind farm, however, the spectral peaks up to about 5 Hz can be seen on all stations. The basement depths for each station are variable based on the seismic refraction data (see Table 1). This suggests that the location of these spectral peaks is not directly related to basement depths, but rather are more related to a source effect of the wind turbines. For example, a soil depth variation of 25 m would result in a shift of about 1 Hz for a primary soil resonance, which is not seen in the data.

2.5. Cross-correlation analysis

Correlation analysis was then performed on these data. The data were detrended and a moving amplitude normalization was performed. A 10% Tukey window was applied to the data. Next, the autocorrelations for each station were calculated and a 40% Tukey window was applied.

Central peaks of the autocorrelations were then extracted, and a Hann window applied. The windowed autocorrelations were then stacked for all stations to provide a windowed and summed autocorrelation for use in the deconvolution of the cross-correlations.

The deconvolved cross-correlations are then computed. The cross-correlations are obtained with respect to a reference station and a Hann window is applied to taper the cross-correlation window. Next, a Butterworth filter is applied from 0.25 Hz to 1 Hz. Damped deconvolutions are then performed using the summed autocorrelation, and a damping of 0.001 is used to obtain the deconvolved cross-correlations. Figure 10a) shows the raw cross-correlations for April 30th, 2020, at 4 AM EST, using ST16 as a reference station, and 10b) shows the deconvolved cross-correlations. It can be seen that the process of deconvolution provides a better time resolution of the cross-correlation signals.

In the deconvolved cross-correlations, there is a clear north to south signal shown for reference station ST16 to the north of the array travelling with a speed of about 2,200 m/s. A Rayleigh wave would have a penetration depth of about half a wavelength, and for a frequency of 1 Hz this would be about 1,100 m. From Table 1, assuming P-wave basement speed of 4,000 m/s and a Poisson solid with $\frac{V_p}{V_s} = 1.73$, this would result in an S-wave basement speed of 2,312 m/s and an approximate Rayleigh wave group speed of 2081 m/s, where $V_R = 0.9V_s$. This is a little lower than the observed speed, but allowing for the lower soil layer speeds, is consistent with what is observed.

Figure 11 shows the deconvolved cross-correlations with respect to seismic station ST16 for one-hour time windows on a) January 8th, 2020, b) December 25th, 2019, and c) December 14th, 2019. The hour blocks of time on these days were selected because they were within selected speed

ranges, and no train signals were recorded. The hour on January 8th had an average wind speed of 5.15 m/s and a wind gust of 11.16 m/s, the hour on December 25th had an average wind speed of 3.3 m/s and wind gust of 5.15 m/s, and the hour on December 14th had an average wind speed of 0.54 m/s and a wind gust of 1.18 m/s. For high wind speeds on January 8th, there are only signals primarily propagating from the north. This suggests that the energy comes predominantly from the north where the large wind farm is located and includes the northern stations of the array. For medium wind speeds on December 25th, there is mostly south-propagating energy. But, there is also north-bound energy near the reference station, indicating that the wind turbines are outputting less power for the medium wind speeds, with the wind turbines farther to the north contributing less. For the low wind speeds on December 14th, there is still an apparent signal coming from the north, but the signal is much less coherent, particularly for the southern portion of the array. The apparent energy coming from the north suggests that, although the average wind speed is 0.54 m/s, and that the northern wind turbines should not be producing energy for speeds below 2 m/s, there must still be some number of turbines turning during this time period.

Figure 12 shows the deconvolved cross-correlations now with respect to reference station ST13 for one-hour time windows on a) January 8th, 2020, b) December 25th, 2019, and c) December 14th, 2019. As is the case for Figure 11a), the high wind speeds show signals propagating from the north, potentially from the large wind turbine farm. For medium wind speeds, while there are predominately signals travelling from the north, there are also some signals propagating from the south. It should be noted that these signals propagate northwards from reference station ST13, which is located at the southern extent of the wind turbine farm. As shown in Figure 11c), for the low wind speeds 12c) shows a deteriorating signal, particularly towards the south, but still with some energy coming from the north.

Figure 13 shows the deconvolved cross-correlations with respect to reference station SFIN for one-hour time windows on a) January 8th, 2020, b) December 25th, 2019, and c) December 14th, 2019. The high wind speed case displays only southward propagating signals. However, unlike Figures 11b) and 12b), medium wind speeds shown in Figure 13b) do not display any energy coming from the south and instead solely displays energy arriving from the north. Low wind speeds in 13c) display mostly incoherent signals but still have some energy coming from the north where the wind turbines are located.

3. Conclusions

Seismic noise from anthropogenic sources has been explored, in particular from wind turbines for data from the Autocorr Seismic Array, which was located just to the west and north of West Lafayette, Indiana in the Midwestern United States from August 2019 to July 2020. The 17-station array consisted of a linear component that extended about 30 km from north to south, and a subarray in the south that was about 10 km in diameter. The northern extent of the array is located within a large, combined wind farm consisting of over 1,100 wind turbines, one of the largest onshore wind farms in the world. To the south of the array, there is an east-west running train tracks with regularly occurring trains. While there is vehicle traffic in the region, the study hours were limited to late at night and early in the morning to minimize the effects of traffic. Except for the southern stations of the Array within several kilometers of the train tracks, the signals propagating from the north dominated over noise signals emanating from trains. We also found that localized spectral peaks in the data developed in amplitude as wind speed increased and did not vary significantly in frequency across the array. Based on previously recorded seismic refraction data in the area, each station had somewhat different basement depths. Since the spectral peaks did not change with station locations, it is inferred that the spectral peaks are more related

to source effects of the wind turbines, and not from the resonances of the soil layers beneath each station. However, a coupling of source effects and propagation effects must also still be occurring.

A difference between this study and some previous seismic studies of wind turbines is that here there are over a thousand wind turbines as part of the large nearby wind farm, as opposed to a much smaller number of wind turbines in previous studies. For example, Neuffer et al. (2019) placed their seismic stations within the vicinity of just five wind turbines. For our study, the spectral peaks attributed to wind turbines could be observed for the full 30 km north-south extent of the seismic array, unlike the 15 km distance range previously found by Stammler and Ceranna (2016). Neuffer et al. (2019) inferred that wind turbine seismic signals will increase as the square root of the number of wind turbines, and this will then increase the observational distance range from the wind turbines.

The anthropogenic seismic noise was then used to perform seismic interferometry, and a coherent Rayleigh wave signal was observed using just one hour time windows. This is important since other studies relied on averaging much longer periods of data to see a clear Rayleigh wave signals. For example, Quiros et al. (2016) used 120 hours of train traffic data. For reference stations in the north and central parts of the seismic array, energy propagated mostly to the south, while some energy propagated to the north. For reference stations to the south of the wind farm, energy propagated mostly to the south, suggesting that the wind turbines are the dominant source of seismic noise in the region. At medium to high wind speeds, these signals are clear, while the signals begin to deteriorate in coherence for low wind speeds.

Data and Resources

The Incorporated Research Institutions for Seismology Portable Array Seismic Studies of the Continental Lithosphere provided the seismic data used in this study (doi: 10.7914/SN/7G_2019). These seismic instruments were set up by Nowack (2019). The atmospheric data was provided by DarkSky, which is a proprietary service, and the specific data used in this study is available as csv files upon email request to Mitchell Spangler (mitchspang@gmail.com).

Acknowledgements

This study was partially supported by National Science Foundation NSR/EAR Grant 1839322. We would like to thank Prof. Wen-Wen Tung for assisting in providing the meteorological data from the DarkSky database.

References

DarkSky. Weather. https://darksky.net/. Last accessed December 1, 2021.

Dybing, S., A. Ringler, D. Wilson, R. Anthony (2019). Characteristics and Spatial Variability of Wind Noise on Near-Surface Broadband Seismometers. *Bulletin of the Seismological Society of America*. **109**, no. 3, 1082–1098. doi: 10.1785/0120180227.

François, L., O. Coutant, P. Boué, L. Pinzon-Rincon, F. Brenguier, R. Brossier, P. Dales, M. Rezaeifar, C. J. Bean (2020). Understanding Seismic Waves Generated by Train Traffic via Modeling: Implications for Seismic Imaging and Monitoring. *Seismol. Res. Lett*. **92**, 287–300, doi: 10.1785/0220200133.

Friedrich, T., T. Zieger, T. Forbriger, J. Ritter. (2018). Locating wind farms by seismic interferometry and migration. *Journal of Seismology*. **22**, doi: 10.1007/s10950-018-9779-0.

Fuchs. F., G. Bokelmann, the AlpArray Working Group (2017). Equidistant Spectral Lines in Train Vibrations. *Seismol. Res. Lett*. **89**, no. 1, 56–66. doi: https://doi.org/10.1785/0220170092 (last accessed Jan. 2022).

Hu, W., R. J. Barthelmie, F. Letson, and S. C. Pryor (2019). Seismic Noise Induced by Wind Turbine Operation and Wind Gusts, *Seismol. Res. Lett.* **91**, 427–437, doi: 10.1785/0220190095.

IGWS Indiana Bedrock https://igws.indiana.edu/Bedrock#:~:text=Bedrock%20is%20exposed%20only%20in,surface%20crossed%20by%20numerous%20drainages (last accessed Jan. 2022).

IGWS Indiana Physiographic Regions https://igws.indiana.edu/ReferenceDocs/Maps/PhysiographicRegions.pdf (last accessed Jan. 2022).

Liu, L, Y. Liu, T. Li, Y. He, Y. Du, Y. Luo. (2021). Inversion of vehicle-induced signals based on seismic interferometry and recurrent neural networks. *Geophysics.* **86**, Q37-Q45, doi: 10.1190/geo2020-0498.1.

Meng, H., Y. Ben-Zion, and C. W. Johnson (2019). Detection of random noise and anatomy of continuous seismic waveforms in dense array data near Anza California, *Geophys. J. Int.* **219**, no. 3, 1463–1473, doi: 10.1093/gji/ggz349.

Neuffer, T., S. Kremers, P. Meckbach, M. Mistler. (2021). Characterization of the seismic wave field radiated by a wind turbine. *Journal of Seismology*. **25**, doi: 10.1007/s10950-021-10003-6.

Neuffer, T., S. Kremers, F. Ralf. (2019). Characterization of seismic signals induced by the operation of wind turbines in North Rhine-Westphalia (NRW), Germany. *Journal of Seismology*. **23**, doi: 10.1007/s10950-019-09866-7.

NS Energy. https://www.nsenergybusiness.com/features/worlds-biggest-onshore-wind-farms/ (Last accessed Jan. 2022).

Nowack, R.L. (2019) Autocorrelation of ambient noise and P-wave coda for crustal structure. International Federation of Digital Seismograph Networks. Dataset/Seismic Network, doi: 10.7914/SN/7G_2019.

Pinzon-Rincon, L., F. Lavoué, A. Mordret, P. Boué, F. Brenguier, P. Dales, Y. Ben-Zion, F. Vernon, C. J. Bean, D. Hollis (2021). Humming Trains in Seismology: An Opportune Source for Probing the Shallow Crust. *Seismol. Res. Lett*. **92**, 623–635, doi: 10.1785/0220200248.

Quiros, D., L. Brown, D. Kim. (2016). Seismic interferometry of railroad induced ground motions: body and surface wave imaging, *Geophys. J. Int.* **205**, 301–313, doi: 10.1093/gji/ggw033.

Riahi, N., and P. Gerstoft (2015). The seismic traffic footprint: Tracking trains, aircraft, and cars seismically, *Geophys. Res. Lett.* **42**, no. 8, 2674–2681, doi: 10.1002/2015GL063558.

Schippkus, S., M. Garden, and G. Bokelmann (2020). Characteristics of the Ambient Seismic Field on a Large-N Seismic Array in the Vienna Basin, *Seismol. Res. Lett.* **91**, 2803–2816, doi: 10.1785/0220200153.

Shapiro, N. M., M. Campillo, L. Stehly, and M. H. Ritzwoller (2005). High-resolution surface-wave tomography from ambient seismic noise, *Science.* **307**, no. 5715, 1615–1618, doi: 10.1126/science.1108339.

Seydoux, L., N. M. Shapiro, J. de Rosny, F. Brenguier, and M. Landès (2016). Detecting seismic activity with a covariance matrix analysis of data recorded on seismic arrays, *Geophys. J. Int.* **204**, no. 3, 1430–1442, doi: 10.1093/gji/ggv531.

Westwood, R., S. Peter, T. Sam. (2015). Seismic monitoring and vibrational characterization of small wind turbines: A case study of the potential effects on the Eskdalemuir International Monitoring System Station in Scotland. *Near Surface Geophysics.* **13**, 115 – 126, doi: 10.3997/1873-0604.2015001.

Withers, M., R. Aster, C. J. Young, E. P. Chael (1996). High-frequency analysis of seismic background noise as a function of wind speed and shallow depth. *Bulletin of the Seismological Society of America*. **86,** no. 5, 1507–1515, doi: 10.1785/BSSA0860051507.

Whaley, J. F., R. F. Blakely, K.K. Like and C.L. James (2002) Seismic Refraction Data for Indiana (Indiana Geological Survey, Point Shapefile): Indiana Geological Survey, Bloomington, IN (Last accessed Dec. 2021).

Zieger, T., K. Ritter (2018). Influence of wind turbines on seismic stations in the upper rhine graben, SW Germany. *Journal of Seismology*, **22**, doi: 10.1007/s10950-017-9694-9.

Station	Soil Depth (m)	Soil Velocity (m/s)	Basement Velocity (m/s)	Closest Point/Average Distance to Station (km)	Number of Points Averaged
ST17/15	25.8 ± 4.6	1862 ± 238	3645 ± 353	1.3/3.5	5
ST16	25.8 ± 4.6	1862 ± 238	3645 ± 353	2.5/3.8	5
ST14	77.6 ± 12.8	1928 ± 241	4313 ± 162	3.7/4.6	4
ST13	63.0 ± 7.3	1930 ± 83	3960 ± 193	0.5/3.0	9
ST12	51.5 ± 7.7	1821 ± 35	4043 ± 205	1.1/2.6	10
ST11	70.8 ± 4.9	1989 ± 34	4086 ± 159	0.6/2.6	10
ST10	87.9 ± 30.8	1821± 89	4425 ±440	1.0/2.5	10
ST08	94.0 ± 13.1	1839± 74	4623 ± 427	0.4/2.1	10
ST01	80.0 ± 14.2	1745 ± 116	4088 ± 275	0.9/2.0	8
SFIN	11.5 ± 2.7	1110 ± 184	2728 ± 115	0.4/1.9	7

Table 1: Averaged depth to bedrock, soil and basement velocities with uncertainties, closest data point, average distance to data points and number of points used for selected seismic stations of the Autocorr Seismic Array. Shallow refraction data were taken from Whaley et al. (2002) and were selected for data quality and distance from each station.

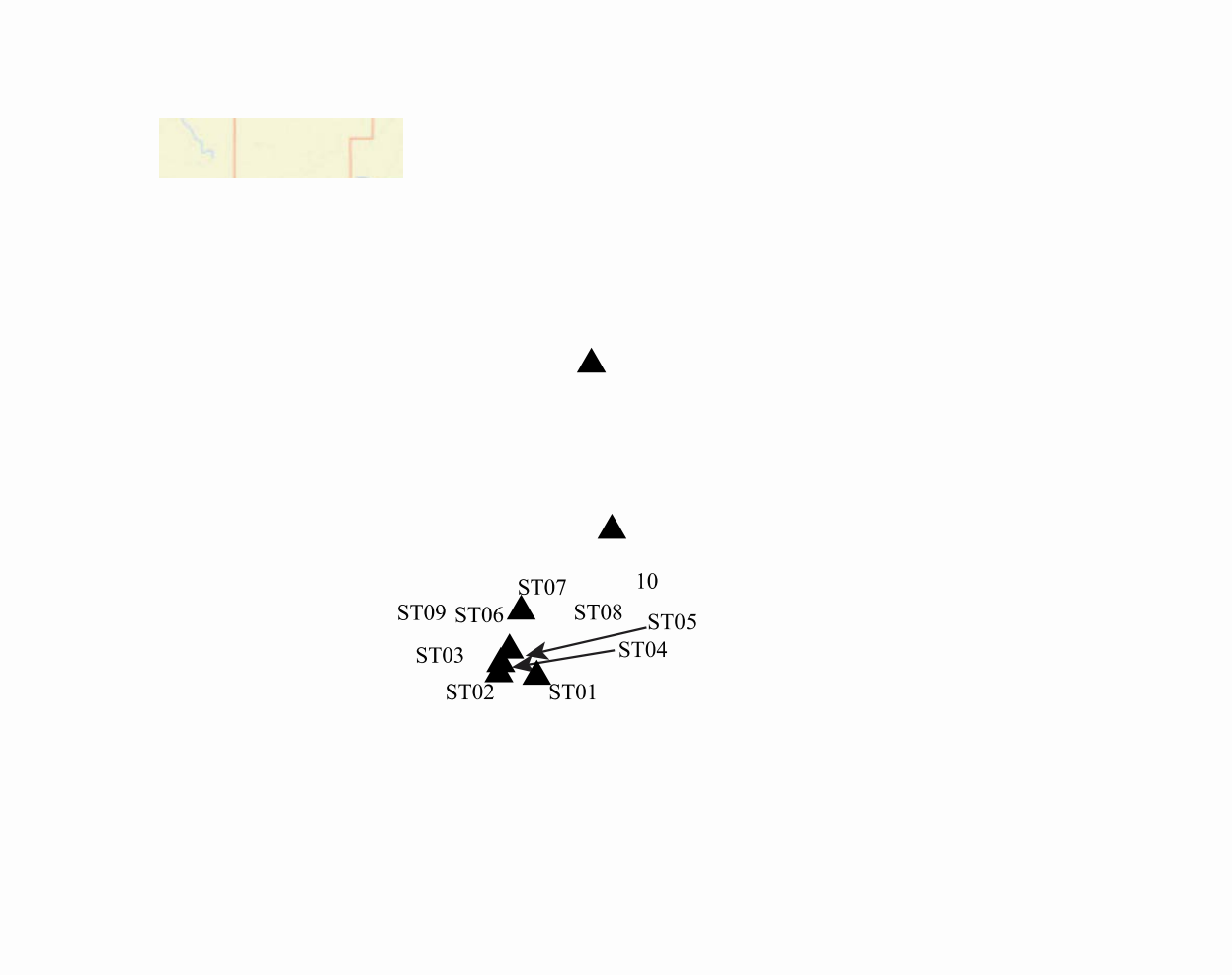

Figure 1. Map of the Autocorr Seismic Array and wind turbines operational during the time of the Autocorr Array deployment. Seismic stations are shown as triangles and wind turbines are shown as red circles. The east-west train tracks are also shown to the south of the array.

a)

b)

Figure 2: a) This shows one of several daily trains passing to the south of the Autocorr Seismic Array, travelling on the East-West train tracks shown in Figure 1. b) This displays a view of a wind turbine and several in the background to the south of ST16 shown in Figure 1.

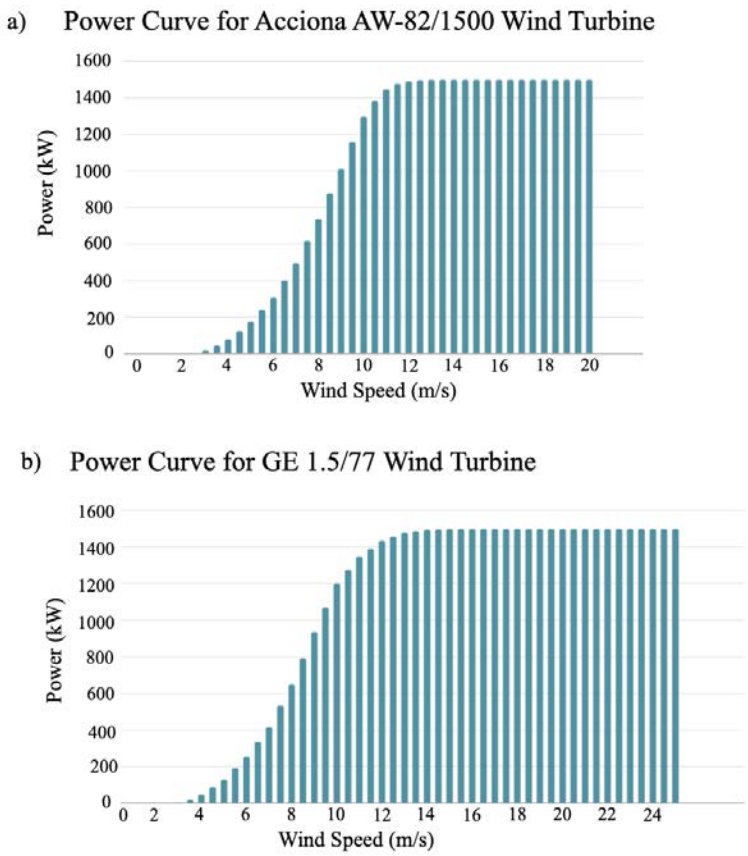

Figure 3: Power curves with respect to wind speed a) for the Acciona AW-82/1500 model for the Meadow Lake II wind turbines and b) for the GE 1.5/77 model for the Meadow Lake III wind turbines. These turbines are nearest to seismic stations ST13, ST14, ST16 and ST15/17. For wind speeds less than 2 m/s, there is no wind turbine power output. For wind speeds greater than 13 m/s for the Acciona and 14 m/s for the GE the power output has reached its maximum for these wind turbines. The Acciona AW-82/1500 has a hub height of 80 meters with a total height, including rotors, of 121 meters. The GE 1.5/77 also has a hub height of 80 meters with a total height, including rotors, of 118.6 meters.

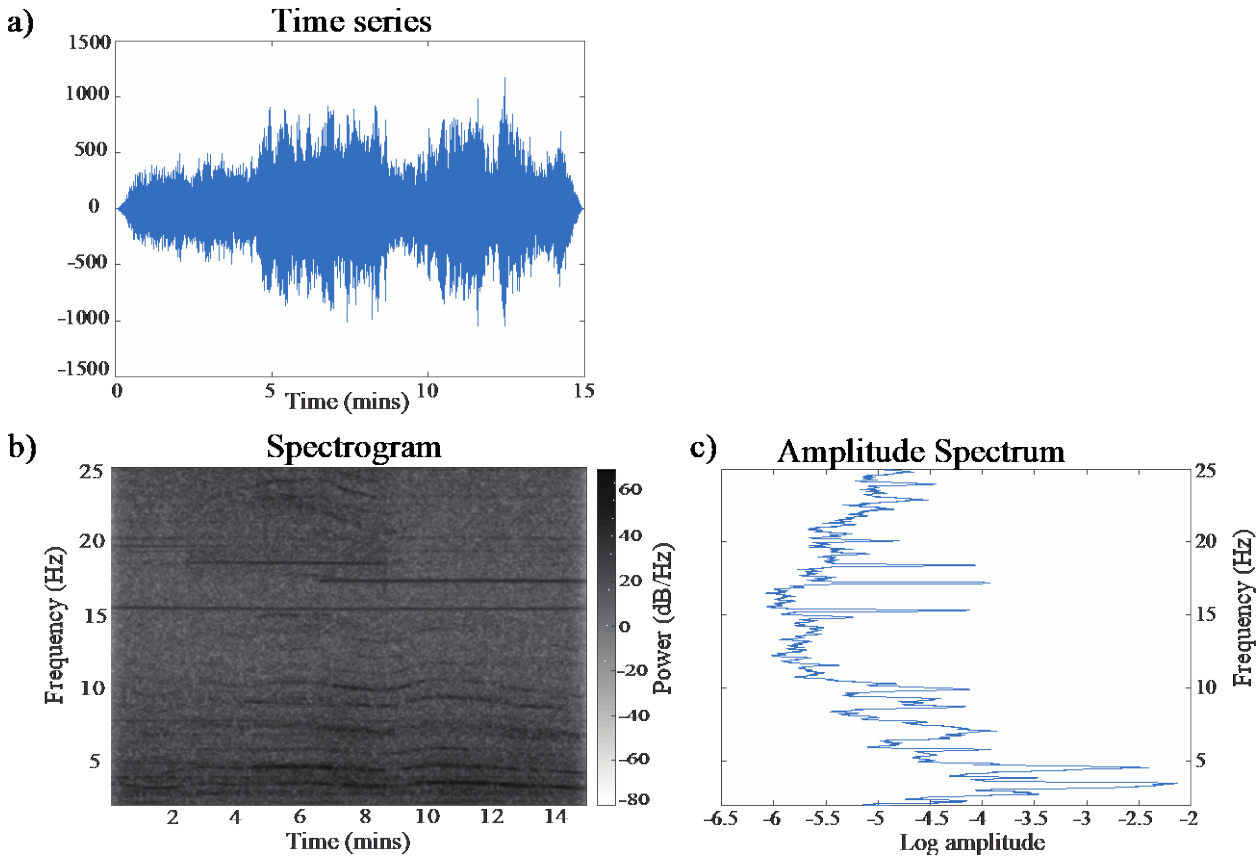

Figure 4: a) Time series b) spectrogram and c) amplitude spectrum for 15 minutes of data recorded at station ST01 of the Autocorr Seismic Array on December 22, 2019 starting at 9:28 UTC. ST01 is one of the southernmost stations in the array and is several kilometers to the north of the east-west train tracks shown in Figure 1. This time window was chosen to show a prominent train signal in the data.

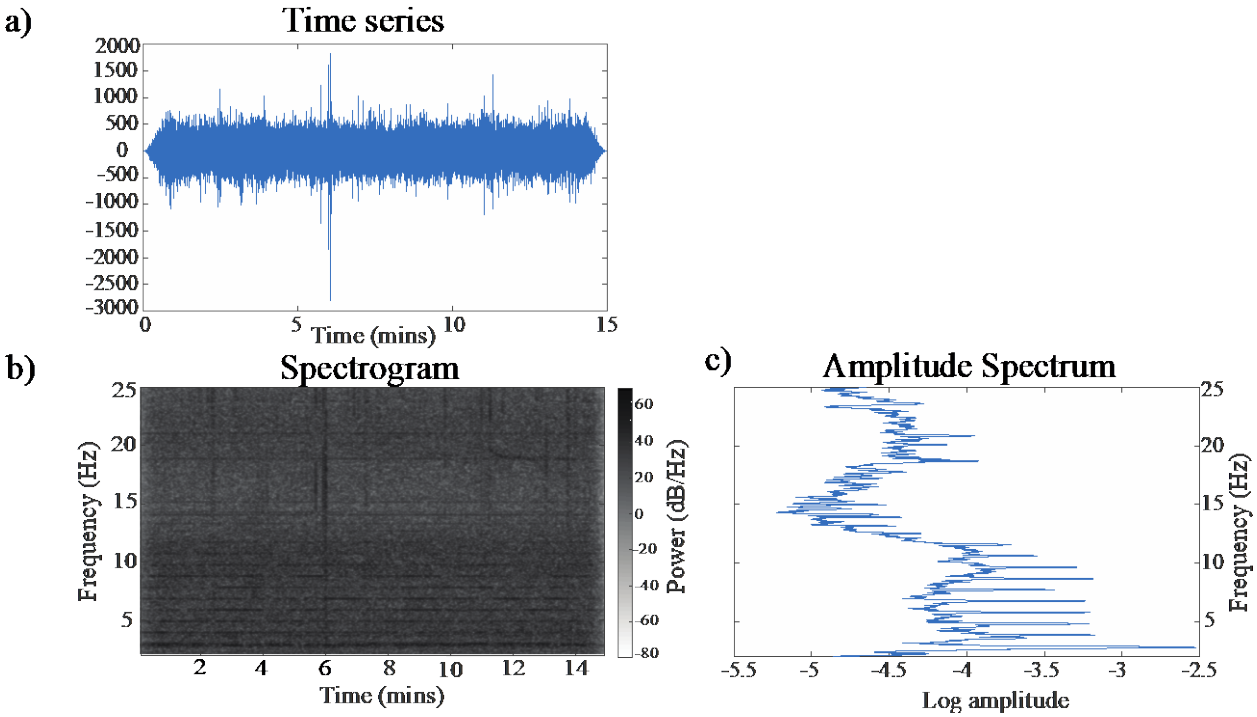

Figure 5: a) Time series b) spectrogram and c) amplitude spectrum for 15 minutes of data recorded at station ST12 of the Autocorr Seismic Array for December 22, 2019 at 9:28 UTC, the same time window shown in Figure 4. ST12 is in the central part of the Autocorr Array. In contrast to the signal recorded at ST01 shown in Figure 5, the train does not dominate the spectra, but rather shows the prominence of the regularly occurring resonance peaks in the spectrum up to 12 Hz.

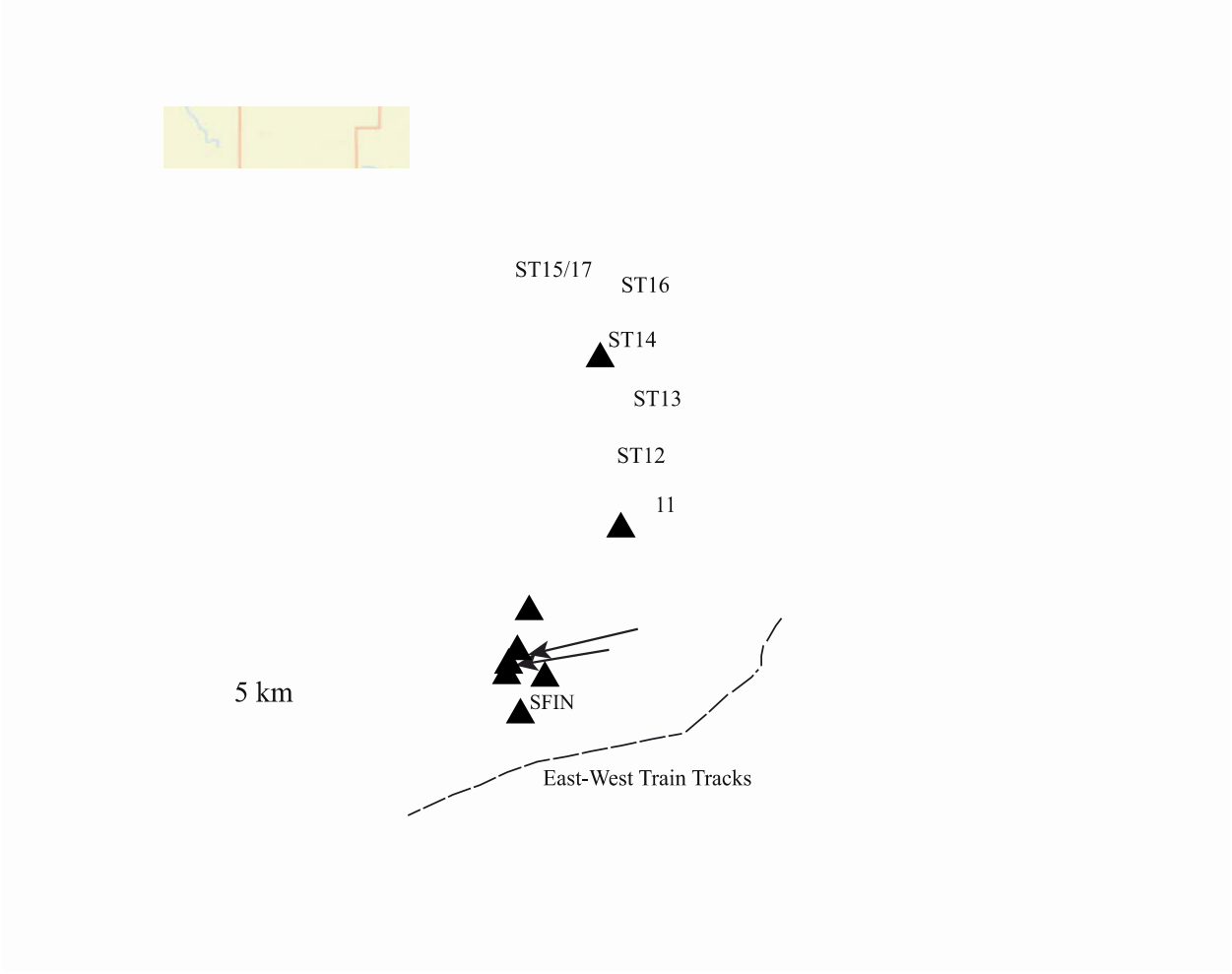

Figure 6: Map of the Autocorr Seismic Array and locations where shallow refraction data were recorded (Whaley et al., 2002). The seismic stations are shown by triangles and the locations of the shallow seismic refraction data are shown by small circles.

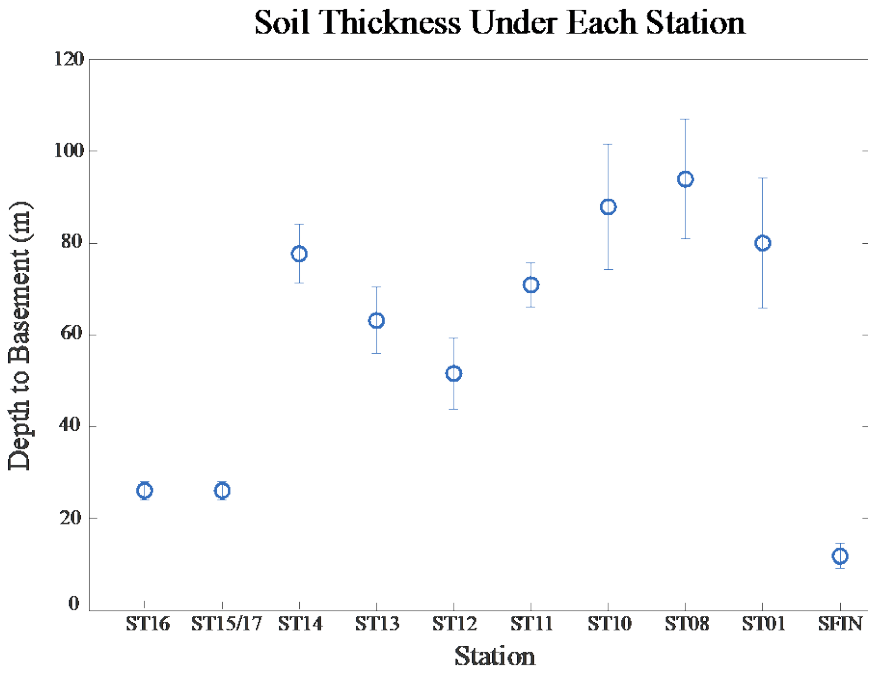

Figure 7: Average basement depths for selected stations of the Autocorr Array and were taken from Whaley et al., (2002). Each basement depth is plotted along with the computed standard error of the mean from Table 1.

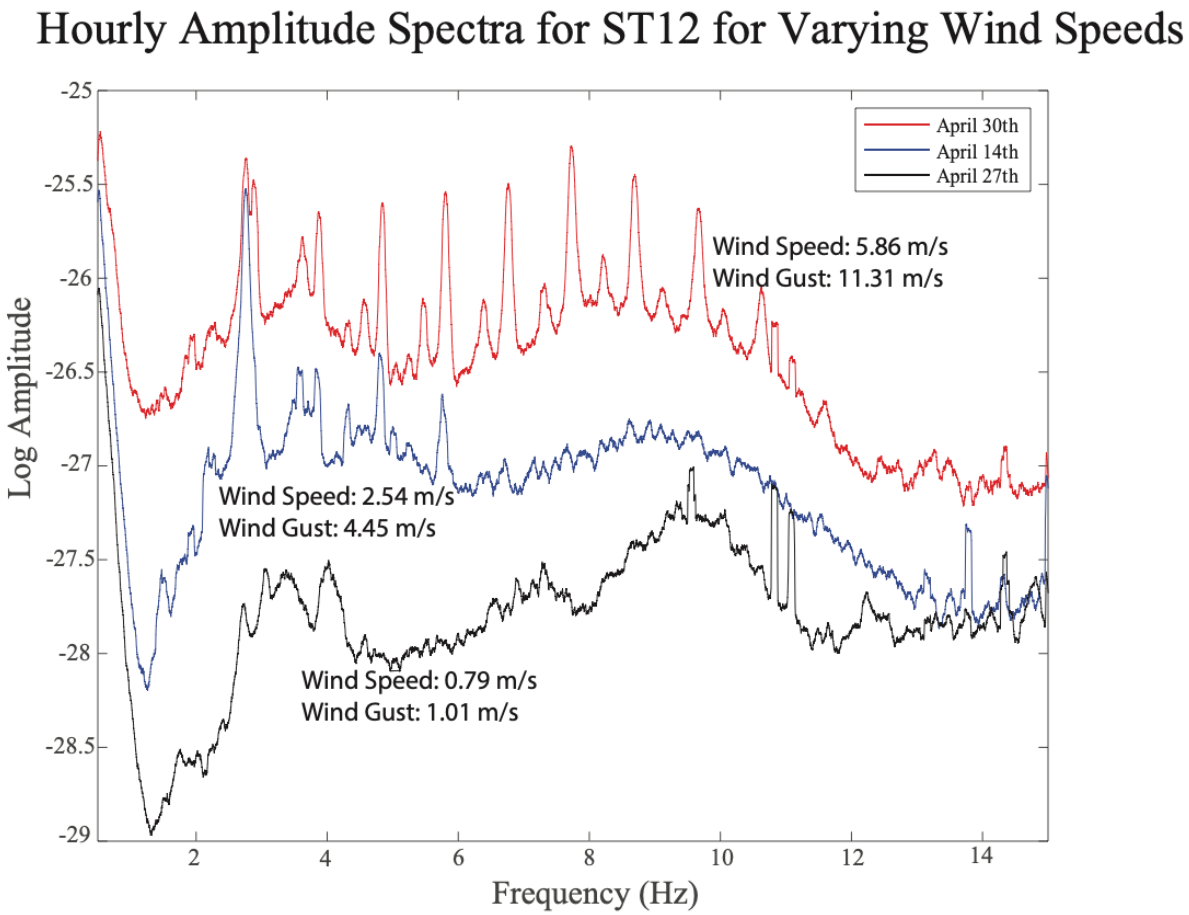

Figure 8: Amplitude spectra for seismic station ST12 for one hour of data starting at 8:00 UTC (3 AM EST) for 3 days, April 27, 14 and 27 of 2020, with different wind speeds and wind gusts. This shows the development of the resonant spectral peaks for increasing hourly wind speeds and wind gusts. The wind data were taken from the Darksky LLC weather data.

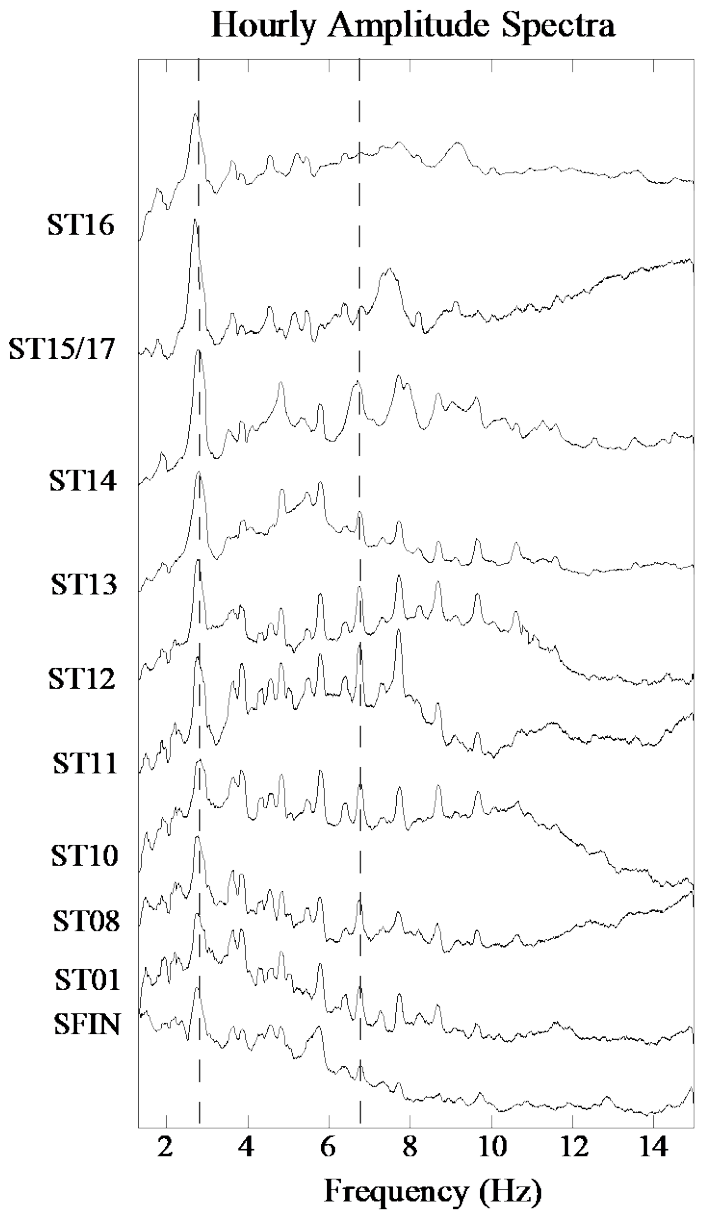

Figure 9: This shows the development of spectral peaks for the spectra of selected seismic stations in the Autocorr Array for an hour on April 30 2020, starting at 8 UTC (4:00 AM EST) For central station ST12, with an average wind speed of 5.86 m/s and a wind gust of 11.31 m/s. This shows that the peaks do not shift significantly at each location.

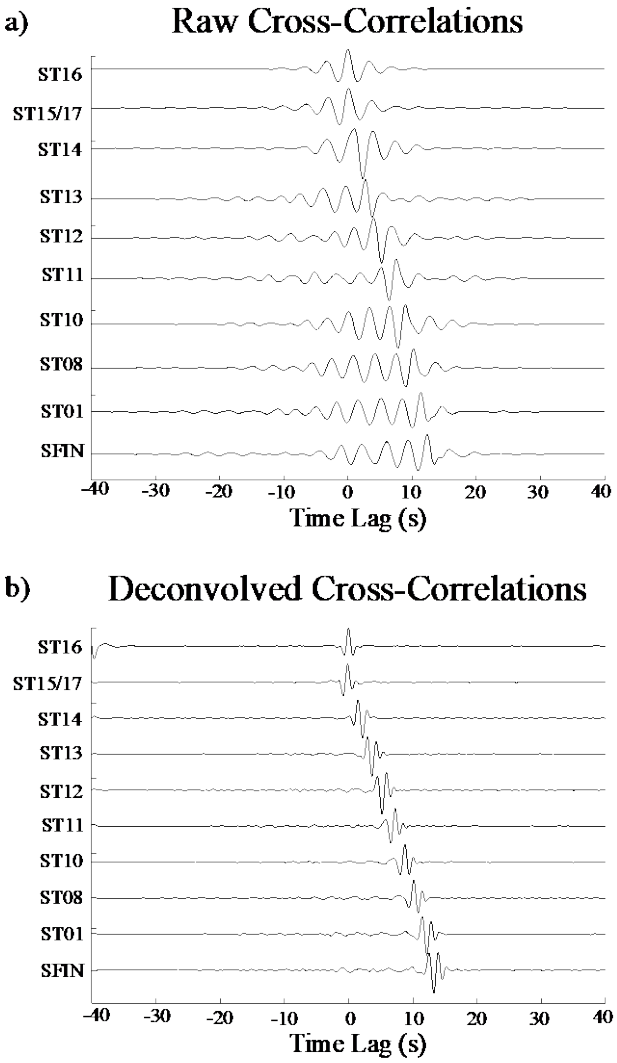

Figure 10: This shows a) the raw cross-correlations and b) the deconvoluted cross-correlations using the average of the array autocorrelations. The data were taken from January 8th, 2020, at 3 AM EST, using ST16 as a reference station. 10b) shows a clearer Rayleigh wave than the raw cross-correlations in 10a).

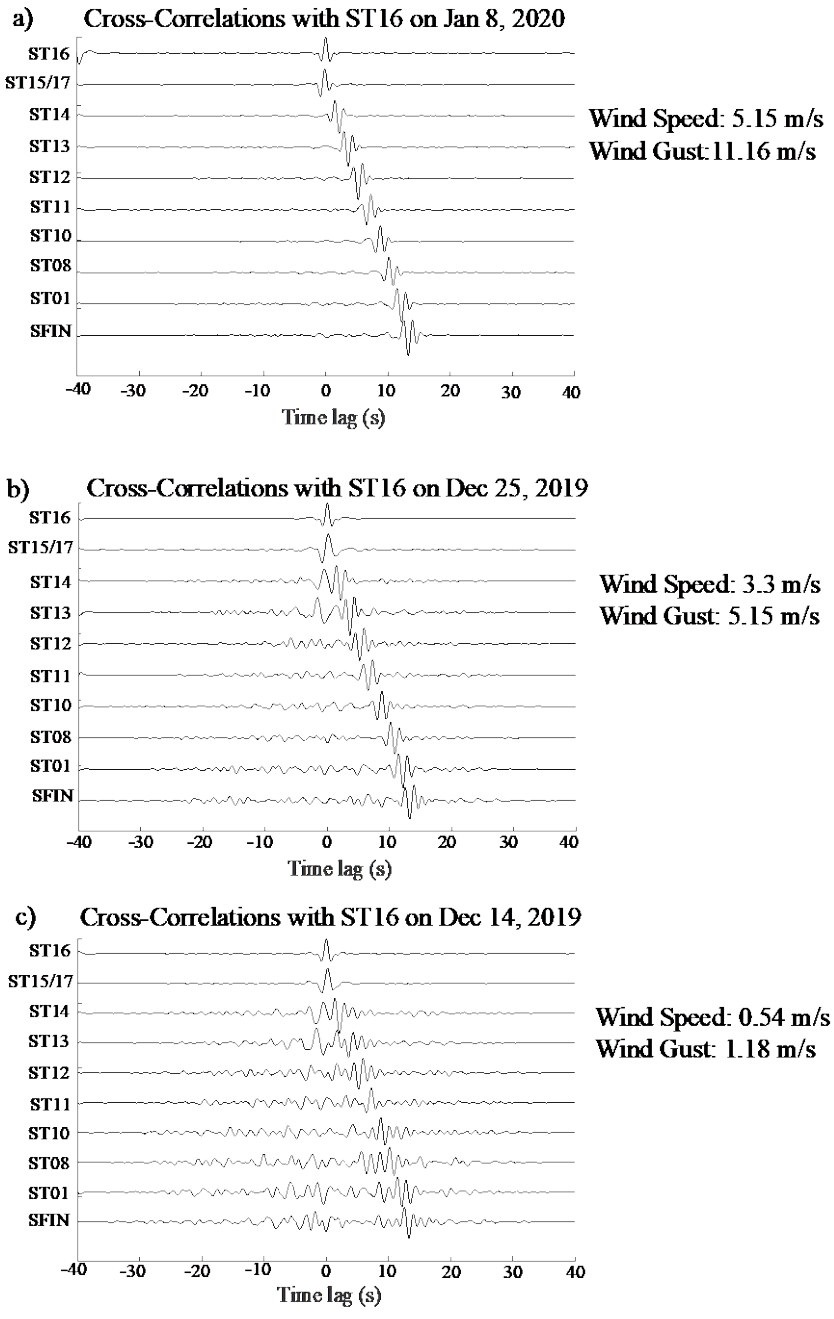

Figure 11: This shows the cross correlations with respect to reference station ST16 for a) January 8, 2020, b) December 25, 2019 and c) December 14, 2019. The north-south extent of the

shown seismic stations is about 29 km. This shows that for high wind speeds, there is no significant signals propagating from the south, indicating that the energy is coming primarily from the large number of wind turbines to the north of the array. For medium wind speeds, there is some north and south propagating energy primarily near the reference station ST16. This may indicate that the larger number of wind turbines to the north of the array are contributing less for the case of medium wind speeds. For lower wind speeds, the correlation results show that the coherence of the signal deteriorates, particularly for stations to the south. Also, the north going energy to the north of ST16 is now more pronounced than the south going energy. This suggests less seismic energy is now propagating from the large number of wind turbines to the north of the array.

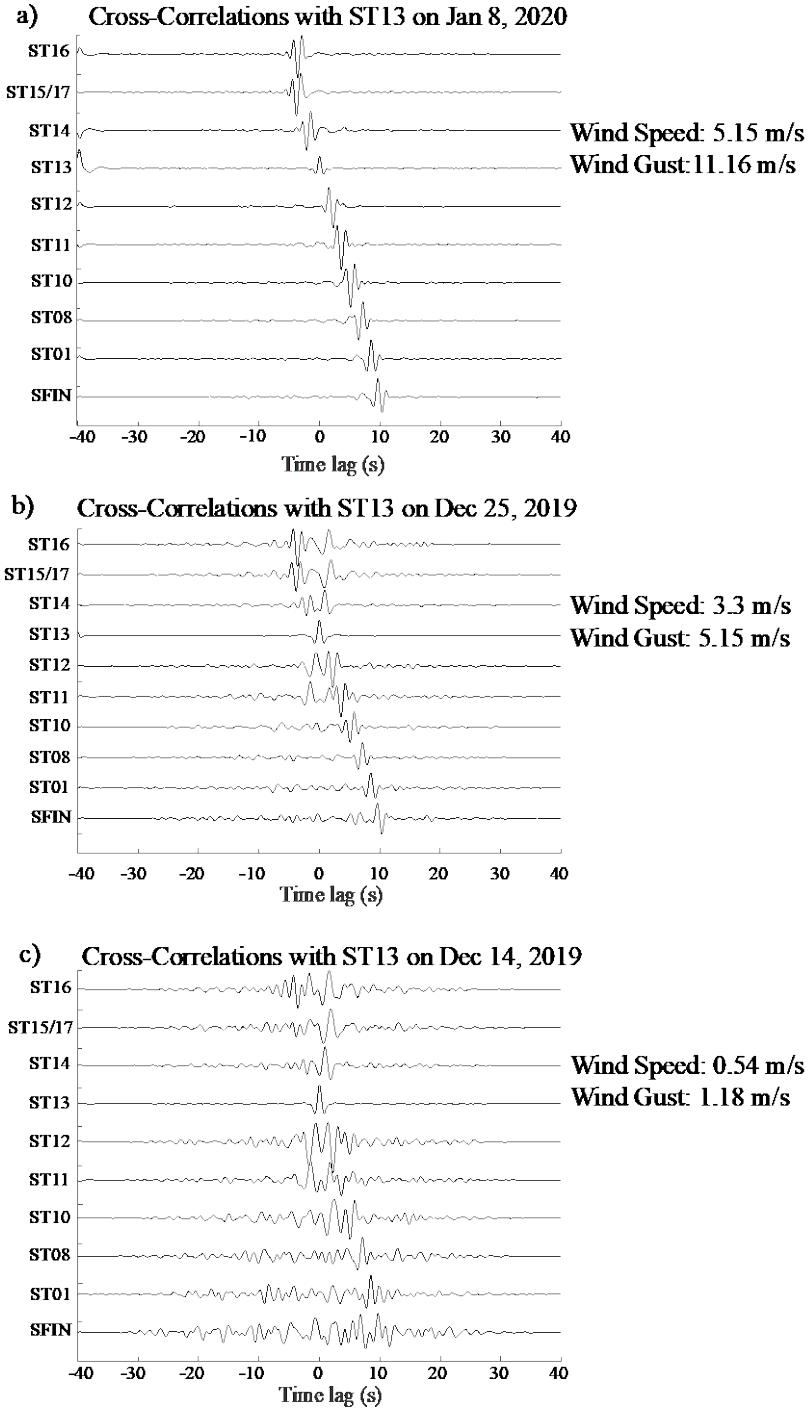

Figure 12: This shows the cross correlations with respect to reference station ST13 for a) January 8, 2020, b) December 25, 2019 and c) December 14, 2019. The north-south extent of the

shown seismic stations is about 29 km. This shows that for high wind speeds, there is no significant signals propagating from the south, indicating that the energy is coming primarily from the large number of wind turbines to the north of the array. For medium wind speeds, there is some north and south propagating energy primarily near the reference station ST13. This may indicate that the larger number of wind turbines to the north of the array are contributing less for the case of medium wind speeds. For lower wind speeds, the correlation results show that the coherence of the signal deteriorates, particularly for stations to the south. Also, the north going energy to the north of ST13 is now more pronounced than the south going energy. This suggests less seismic energy is now propagating from the large number of wind turbines to the north of the array.

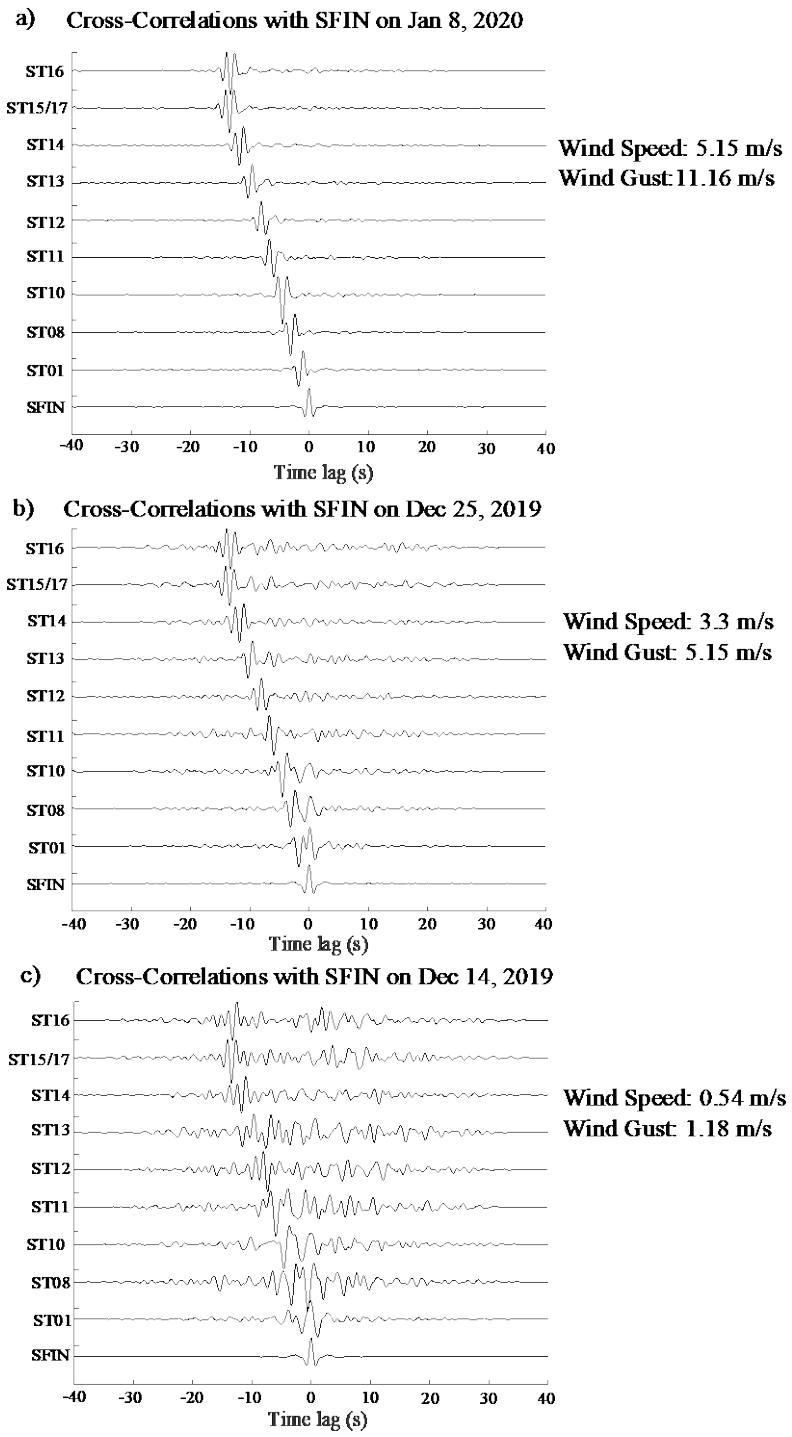

Figure 13: This shows the cross correlations with respect to refernce station SFIN for a) January 8, 2020, b) December 25, 2019 and c) December 14, 2019. The north-south extent of the shown seismic stations is about 29 km. This shows that for high wind speeds, there is no significant

signals propagating from the south, indicating that the energy is coming primarily from the large number of wind turbines to the north of the array. For medium wind speeds, there is some north and south propagating energy primarily near the reference station ST13. This may indicate that the larger number of wind turbines to the north of the array are contributing less for the case of medium wind speeds. For lower wind speeds, the correlation results show that the coherence of the signal deteriorates, particularly for stations to the south. Also, the north going energy to the north of SFIN is now more pronounced than the south going energy. This suggests less seismic energy is now propagating from the large number of wind turbines to the north of the array.